Available online at www.sciencedirect.com
ScienceDirect
Trans. Nonferrous Met. Soc. China 34(2024) 737−754
Transactions of Nonferrous Metals Society of China
www.tnmsc.cn

Effects of Cu content and heat treatment process on microstructures and mechanical properties of Al−Si−Mg−Mn−*x*Cu cast aluminum alloys

Zhi-hong JIA[1,2], Guang-wen ZHOU[2], Hong-yu ZHOU[3], Fei LIU[4],
Li-peng DING[1], Yao-yao WENG[5], Kai-yun XIANG[2], Hai-dong ZHAO[4]

1. Key Laboratory for Light-weight Materials, Nanjing Tech University, Nanjing 211816, China;
2. College of Materials Science and Engineering, Chongqing University, Chongqing 400044, China;
3. School of Materials Science and Engineering, Jiangsu University, Zhenjiang 212013, China;
4. National Engineering Research Center of Near-net-shape Forming for Metallic Materials, South China University of Technology, Guangzhou 510640, China;
5. School of Materials Science and Engineering, Nanjing Institute of Technology, Nanjing 211167, China

Received 28 August 2022; accepted 6 May 2023

Abstract: The effects of Cu content and heat treatment process on the microstructures and mechanical properties of a series of Al−Si−Mg−Mn−*x*Cu cast aluminum alloys prepared by the vacuum die casting process were investigated by three-dimensional X-ray microscopy, optical microscopy, scanning electron microscopy, transmission electron microscopy and microhardness testing. It was found that the number density and size of gas porosities increase with increasing Cu content. However, the Cu addition will promote the formation of Cu-containing primary phases (Q-$Al_5Cu_2Mg_8Si_6$ and θ-Al_2Cu) during the solidification, which will improve the properties of the alloys. Five different primary phases were observed, namely eutectic Si, α-Al(Fe,Mn)Si, β-Mg_2Si, Q-$Al_5Cu_2Mg_8Si_6$, and θ-Al_2Cu phases. With increasing the Cu content, the θ phase area fraction increases significantly, while the α-Al(Fe,Mn)Si phase area fraction decreases initially, followed by a slight increase, with the Q phase area fraction displaying the opposite trend relative to α-Al(Fe,Mn)Si phase. These primary phases present different evolution rules during heat treatment process. During subsequent aging, the synergic effect of precipitating Q' and θ' phases can significantly increase the alloy hardening response.

Key words: Al−Si cast alloy; vacuum die casting; heat treatment; microstructure; mechanical properties; primary phases

1 Introduction

Al−Si cast alloys are the most widely used castings in the automotive and aerospace industries due to their excellent castability, good corrosion resistance and cutting performance [1,2]. These alloys are often used in the manufacturing of cylinder blocks, cylinder heads and pistons of automobile engines [3]. The mechanical properties of the Al−Si cast alloys depend on many factors, including the alloy composition, casting method, heat treatment process, etc. [4,5]. Casting defects, including pores and inclusions, represent the most common challenges to acceptable materials performance. These defects have a deleterious influence on the alloy mechanical properties, especially the ductility. Thus, decreasing the level of porosity is essential for the application of the cast components [6,7]. The vacuum die casting process

Corresponding author: Zhi-hong JIA, Tel: +86-25-83589187, E-mail: zhihongjia@njtech.edu.cn;
Li-peng DING, Tel: +86-25-83589187, E-mail: lipeng.ding@njtech.edu.cn
DOI: 10.1016/S1003-6326(23)66431-3

is one of the most promising methods for decreasing gas entrapment during die filling, thereby limiting the number of porosities. This process has been extensively applied in the manufacturing of complex castings.

Present-day main approaches to controlling the microstructures and properties of Al−Si cast alloys are microalloying and heat treatment processes [8,9]. In general, Mg, Cu, Fe, and Mn are the main alloying elements in Al−Si alloys, forming various secondary phases during the solidification [10,11]. The following intermetallic phases may be present and play an important role in determining the mechanical properties of these alloys [5,12,13]: α-$Al_{15}(Fe,Mn)_3Si_2$, β-Al_5FeSi, π-$Al_8Mg_3FeSi_6$, Mg_2Si, θ-Al_2Cu, Q-$Al_5Cu_2Mg_8Si_6$ and S-Al_2CuMg. Fe is one of the main impurities in Al−Si alloys. As the solubility of Fe in the α(Al) matrix is rather low [14], this element can readily form coarse β-Al_5FeSi brittle intermetallic compounds with needle-like morphology and sharp edges, causing a reduction in the alloy ductility [15]. This harmful effect of Fe is usually neutralized by the introduction of Mn [16]. The addition of a suitable amount of Mn can transform the needle-like β-Al_5FeSi phase into the Chinese-script α-$Al_{15}(Fe,Mn)_3Si_2$ phase, improving the alloy mechanical properties [17,18]. The addition of Cu leads to the formation of the θ-Al_2Cu phase with block-like and eutectic-like morphologies [19,20]. During aging treatment, the formation of the θ' phase can greatly enhance the strength of the alloys [21]. When Mg and Cu elements coexist in Al−Si cast aluminum alloys, the quaternary Q-$Al_5Cu_2Mg_8Si_6$ phase is formed [22]. CÁCERES et al [23] reported increased levels of pore defects in an Al−Si−Cu−Mg alloy (A356.2) when increasing the Cu content. However, due to the limitations of the SEM in probing the 3D morphology of the gas porosities, there is still some controversy regarding the effect of Cu on these porosities in Al−Si cast alloys.

Regarding the heat treatment process, the main purpose of solution treatment is to spheroidize the eutectic Si particles and thus improve the alloy plasticity [24,25]. During this treatment, the secondary phases such as the θ-Al_2Cu, β-Mg_2Si and Q-$Al_5Cu_2Mg_8Si_6$ phases are dissolved to produce a supersaturated solid solution, which facilitates the formation of nano-sized precipitates during a subsequent aging treatment [9,26]. By contrast, the α-Fe phase is virtually unaffected by the solution treatment, due to its highly stable structure [27,28].

Up until now, most research involving the Al−Si cast alloys has been restricted to the conventional casting procedure, while the evolution in materials microstructure and properties for a vacuum die cast Al−Si alloy during the full casting and heat treatment procedures is still not fully understood. Especially, the influence of Cu on the evolution of secondary phase particles is lacking. The aim of the present study is to investigate the effects of Cu addition and heat treatment on the microstructures and mechanical properties of Al−Si cast alloys. A series of Al−Si−Mg−Mn−xCu cast alloys were prepared by the vacuum die casting process and heat treated under different conditions. The microstructures of these four alloys under as-cast, solutionized and aged conditions were analyzed in detail, thereby providing support for the design and production of the new Al−Si casting alloys.

2 Experimental

2.1 Materials and processes

Four Al−Si−Mg−Mn cast alloys with different Cu contents were prepared by a TOYO BD−250V5 cold chamber HPDC machine equipped with a vacuum system. A commercial Al−Si−Mg−Mn alloy and an Al−40wt.%Cu master alloy were used as the starting materials. The raw materials with the ratio adjusted via a burn loss consideration were melted in an electric resistance furnace at (710±10) °C for 20 min and then subjected to degassing with Ar (99.999%) at a pressure of 90 MPa and a fast shot speed of 2.0 m/s. The actual chemical composition of each alloy was determined using an inductively coupled plasma emission spectrometer (ICP-OEC) and a direct-reading spectrometer, with the results shown in Table 1.

The four cast alloys with different Cu contents (labeled A1−A4 in the rest of this work, and the number rising with Cu content) were initially solution-treated at 530 °C for 4 h, and then immediately quenched in water to obtain a supersaturated solid solution. Following this, the alloys were artificially aged in an oil bath furnace at 185 °C for different durations.

Table 1 Actual chemical compositions of four alloys examined in this study (wt.%)

Alloy	Si	Mg	Mn	Fe	Cu	Zn	Ti	Sr	Al
A1	11.48	0.333	0.518	0.057	0.111	0.027	0.077	0.003	Bal.
A2	11.38	0.347	0.539	0.070	0.321	0.024	0.078	0.002	Bal.
A3	11.16	0.316	0.547	0.069	0.676	0.023	0.080	0.003	Bal.
A4	10.86	0.307	0.568	0.067	0.879	0.021	0.079	0.002	Bal.

2.2 Microstructure characterization

The size distribution and volume fraction of pores in the four alloys were assessed by a Zeiss Xradia 620 Versa 3D X-ray microscope (CT). The operating voltage and current were chosen to be 50 kV and 90 μA, respectively. Finally, the 3D morphology of the pores was reconstructed with the 2701 scanning slice images using Dragon fly Pro software.

The Vickers microhardness measurements were carried out using the 310HVS−5 digital display small-load Vickers hardness tester with testing loads of 500 g and a dwell time of 15 s. In order to obtain reliable values, 14 hardness values per condition were tested. The metallographic microstructure of each alloy was examined using a Zeiss optical microscope. The microstructure observations were conducted on a scanning electron microscope (FIB/SEM, ZEISS AURIGA) with an energy disperse spectroscopy (EDS) detector, and a transmission electron microscope (TEM, Tecnai G2 F20) operated at 200 kV. The TEM specimens were thinned using a twin-jet electrochemical equipment at a voltage of 15 V employing a 70 vol.% methanol and 30 vol.% nitric acid solution cooled down to approximately −30 °C. Finally, in order to fully understand the primary phase in the alloy, the 3D morphologies of these phases were observed and analyzed. The detailed preparation process of powder samples has been described in a previous work [29].

3 Results and discussion

3.1 As-cast microstructure

3.1.1 Defects analysis

Casting defects represent the most common challenge to cast alloy performance. SEM images showing the cross-sectional microstructures of the four as-cast alloys examined in this work are displayed in Fig. 1. A low number of small pores are observed throughout, but no large defects are detected. Since the SEM investigation only presents the two-dimensional distribution of the pores, an X-ray microscope was used to obtain the real pore distribution in three-dimensional space for the alloys. These results are displayed in Fig. 2. Gas porosities, appearing with varying size and separation, are revealed in all four alloys. The detailed statistical results are given in Fig. 3 and Table 2. When the Cu content increases from 0.111 wt.% to 0.879 wt.%, the pore number density rises from 1.40×10^{-4} to 3.36×10^{-4} μm^{-3}, about 140% increment, and the pore volume fraction also increases from 0.09% to 0.32%. The average pore sizes in the four alloys are measured to be 33.2, 62.0, 122.1 and 61.7 μm, respectively. The A3 alloy has the largest pore size compared with the other three alloys, which is probably due to the variation during casting. It may be deduced from these observations that an increasing alloy Cu content can increase the number density, volume fraction and probably also the size of the pores.

3.1.2 Thermodynamic calculations

The equilibrium phase diagrams of the four cast alloys were calculated using the Thermo-Calc 2019 software, with the results shown in Fig. 4. Six secondary phases are observed: α-Al_8Fe_2Si, β-Al_5FeSi, Q-$Al_5Cu_2Mg_8Si_6$, eutectic Si, Mg_2Si and θ-Al_2Cu. Table 3 summarizes the molar fraction of the different equilibrium phases at 20 °C. With increasing the Cu content, the molar fraction of the θ-Al_2Cu phase is found to increase. The molar fractions for the Q-$Al_5Cu_2Mg_8Si_6$ phase in the A2, A3 and A4 alloys are similar and higher than that in the A1 alloy, implying that the presence of this phase soon reaches the saturation as the alloy Cu content is raised.

3.1.3 Secondary phase distribution

The metallographic microstructures of the four cast alloys are shown in Fig. 5. The as-cast alloys are heterogeneous, containing α(Al) matrix grains,

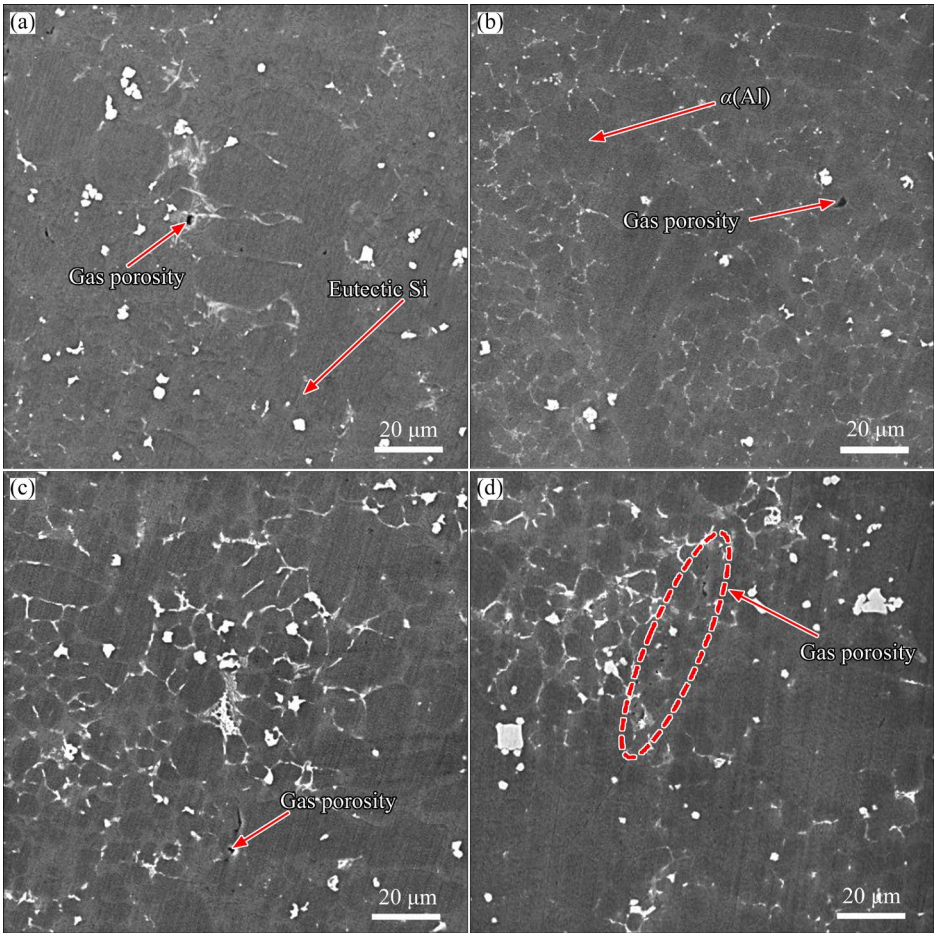

Fig. 1 SEM images of four as-cast alloys: (a) A1; (b) A2; (c) A3; (d) A4

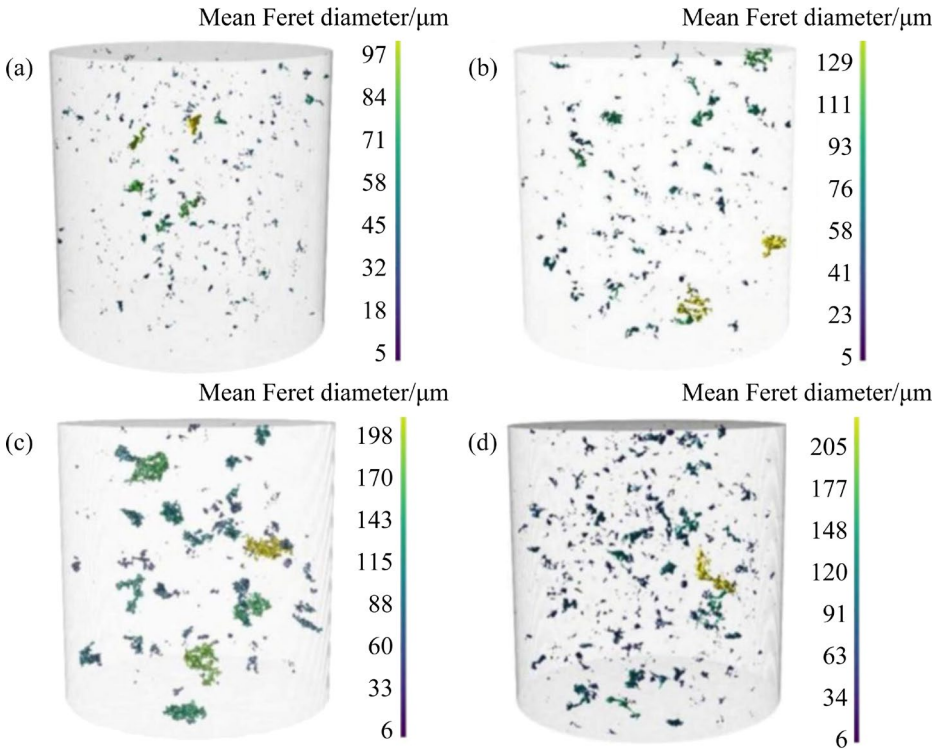

Fig. 2 3D morphology distribution of casting defect holes in four as-cast alloys: (a) A1; (b) A2; (c) A3; (d) A4

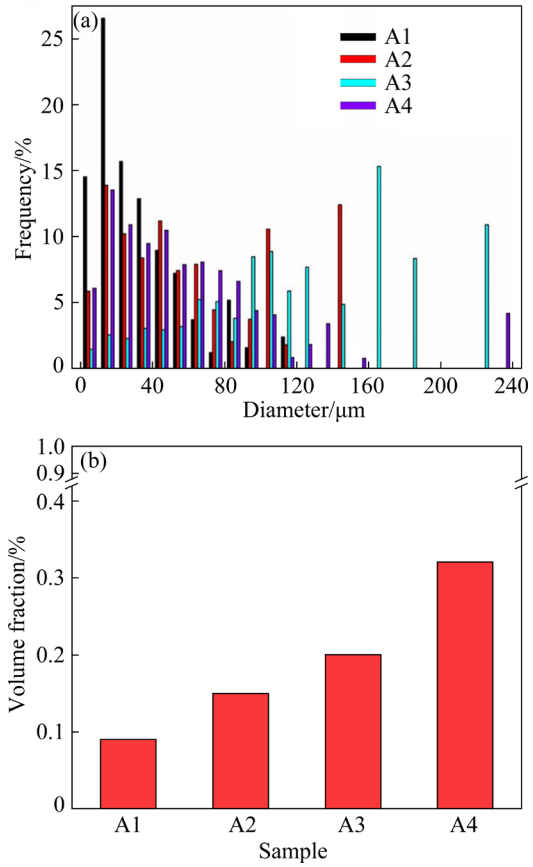

Fig. 3 Size distribution (a) and volume fraction (b) of alloy pores

Table 2 Statistical results for pores obtained from 3D perspective views of four alloys

Alloy	Pore number density/μm^{-3}	Mean diameter/μm	Volume fraction/%
A1	1.40×10^{-4}	33.2	0.09
A2	1.72×10^{-4}	62.0	0.15
A3	1.93×10^{-4}	122.1	0.20
A4	3.36×10^{-4}	61.7	0.32

eutectic Si and intermetallic particles. The α(Al) matrix (bright contrast) displays two different morphologies, small dispersed α(Al) grains appearing in petal morphology and large dendritic grains. The eutectic Si is dispersed around the α(Al) matrix grains. Under the effect of Sr modification and a fast solidification rate in a high-pressure environment, the eutectic Si (black contrast) exhibits fibrous and short rod-like morphologies, closely interconnected as a spatial network. The intermetallic particles (dark gray) display granular or Chinese-script morphologies in the interdendritic area. No clear difference can be detected for the four different alloys at this stage of evolution.

Figure 6 shows the electron backscattered SEM images of the four as-cast alloys. Different

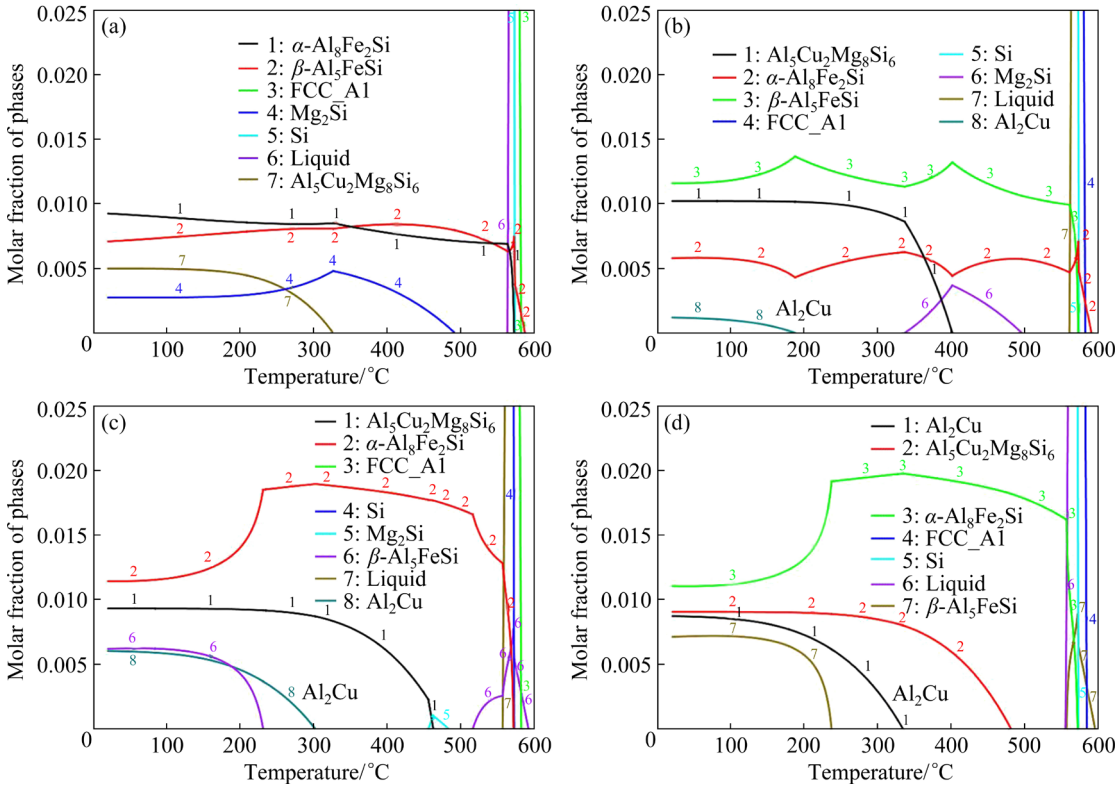

Fig. 4 Calculated molar fractions of equilibrium phase obtained using Thermo-Calc 2019 software: (a) A1; (b) A2; (c) A3; (d) A4

Table 3 Molar fractions of different equilibrium phases at 20 °C predicted by Thermo-Calc 2019

Alloy	$Al_5Cu_2Mg_8Si_6$	α-Al_8Fe_2Si	β-Al_5FeSi	Al_2Cu	Mg_2Si
A1	0.501	0.927	0.708	−	0.271
A2	1.019	0.578	1.153	0.110	−
A3	0.927	1.149	0.620	0.605	−
A4	0.908	1.107	0.716	0.865	−

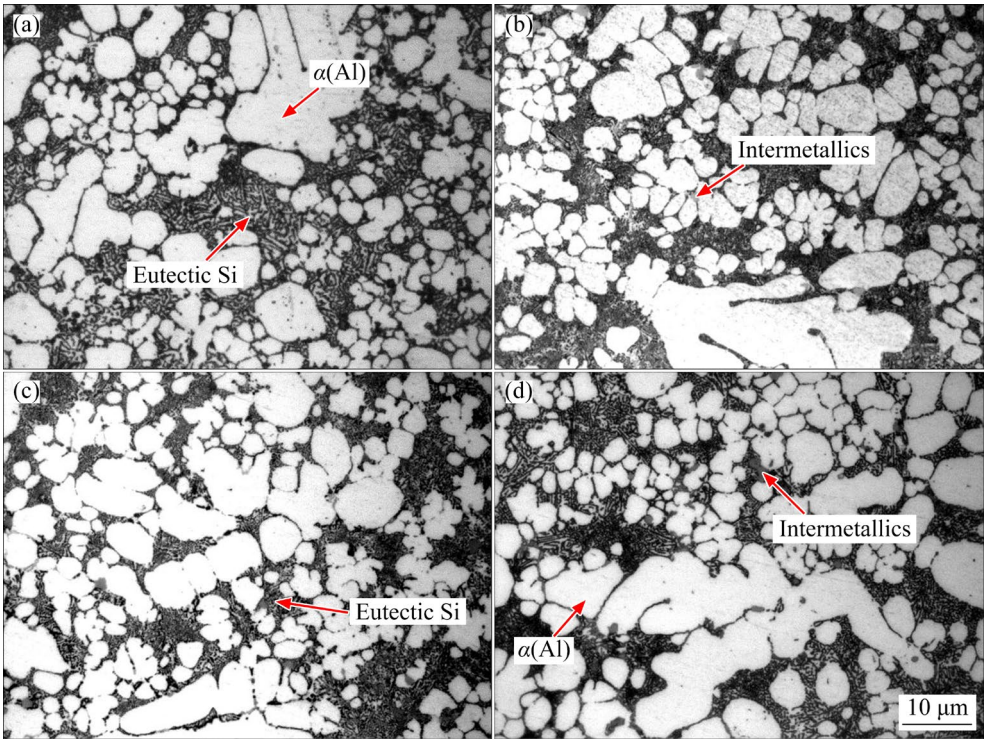

Fig. 5 Typical optical micrographs of four as-cast alloys: (a) A1; (b) A2; (c) A3; (d) A4

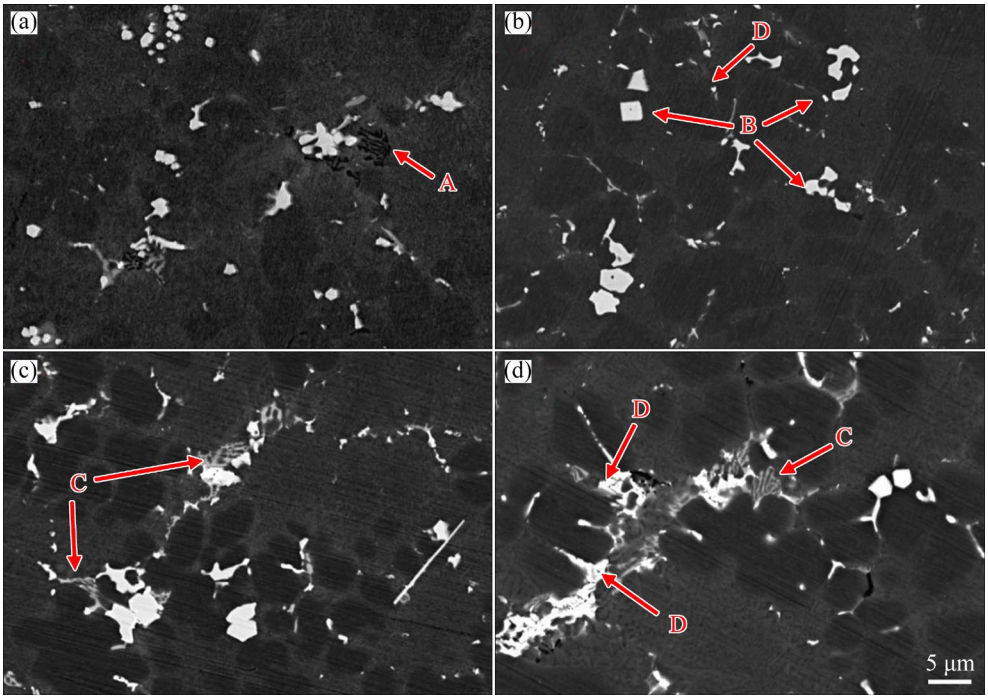

Fig. 6 Backscattered electron SEM (BSE−SEM) micrographs of four as-cast alloys: (a) A1; (b) A2; (c) A3; (d) A4

primary phases with different morphologies, sizes and compositions are observed. Four different primary phases (labelled A, B, C and D at the outset) can be identified: the A phase (black contrast) displays Chinese-script morphology, the B phase (light white contrast) has a variety of morphologies, such as Chinese-script, polyhedral, granular and needle-like morphologies, the C phase (gray contrast) displays Chinese-script and rod-like morphologies, and finally, the D phase (bright white contrast) displays the two typical eutectic-like and block-like morphologies. The D phase is formed in the A2, A3 and A4 alloys, and the number density of this phase increases with the increase of Cu content.

To identify the type of these primary phases, backscattered electron and EDS elemental measurements of the phases formed in the A1 and A4 alloys were performed, with the results shown in Fig. 7. Enlarged EDS elemental maps of the primary phase with regular square-shaped and Chinese-script morphologies are shown in Fig. 8. The A phase is found to contain Mg and Si, the B phase contains Al, Si, Mn and Fe, the C phase contains Al, Si, Mg and Cu, and the D phase contains Al and Cu. The SEM images with point EDS and the chemical compositions (at.%) of the intermetallic compounds are shown in Fig. 9 and Table 4, respectively. By analyzing the stoichiometry of different intermetallic phases, the A, B, C and D phases can be identified as β-Mg_2Si, α-Al(Fe,Mn)Si, Q-$Al_5Cu_2Mg_8Si_6$ and θ-Al_2Cu, respectively. Almost all of these intermetallic phases are observed to adhere to the eutectic Si, being symbiotic with this phase. This behavior probably reflects preferential nucleation and growth of intermetallic phases on the eutectic Si during solidification.

Figure 10 shows 3D morphologies of the various primary phases. These morphologies are

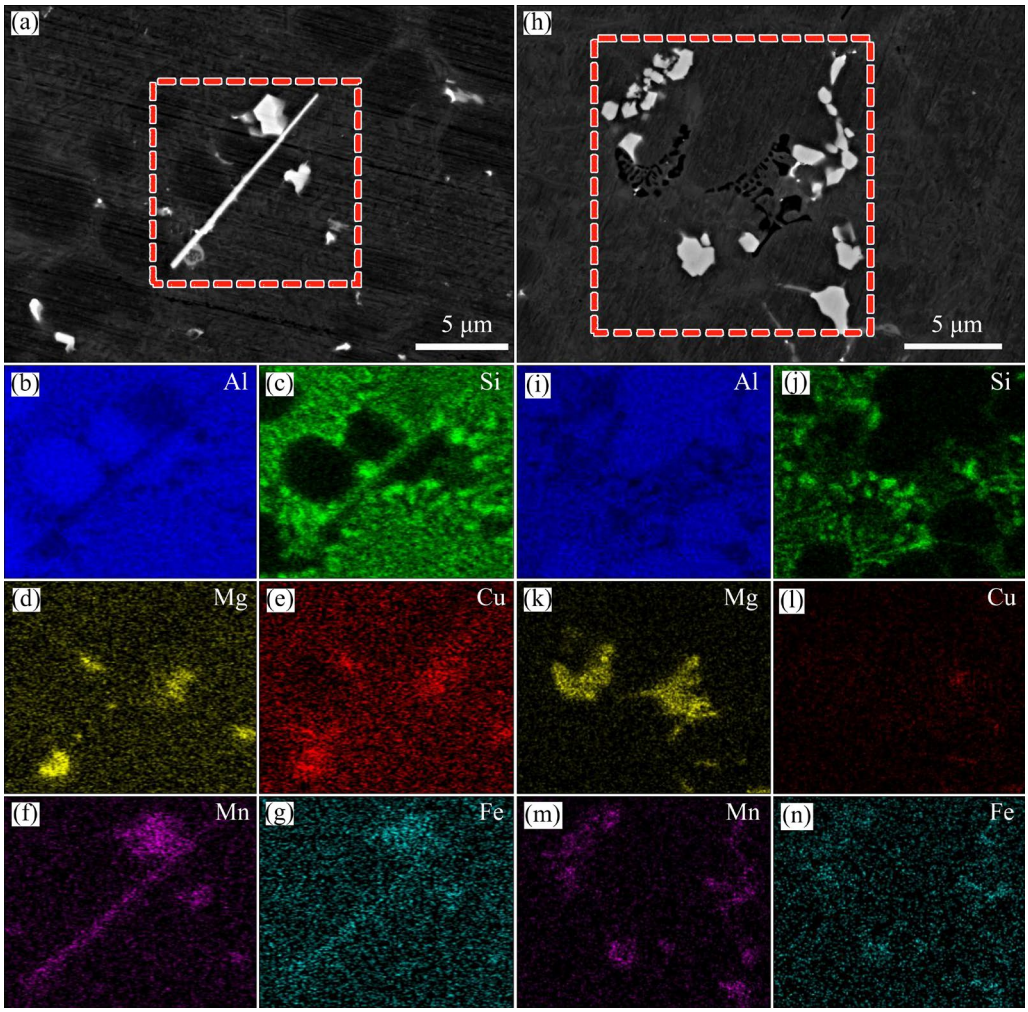

Fig. 7 BSE−SEM images and EDS mappings of primary phases of as-cast A1 (a−g) and A4 (h−n) alloys

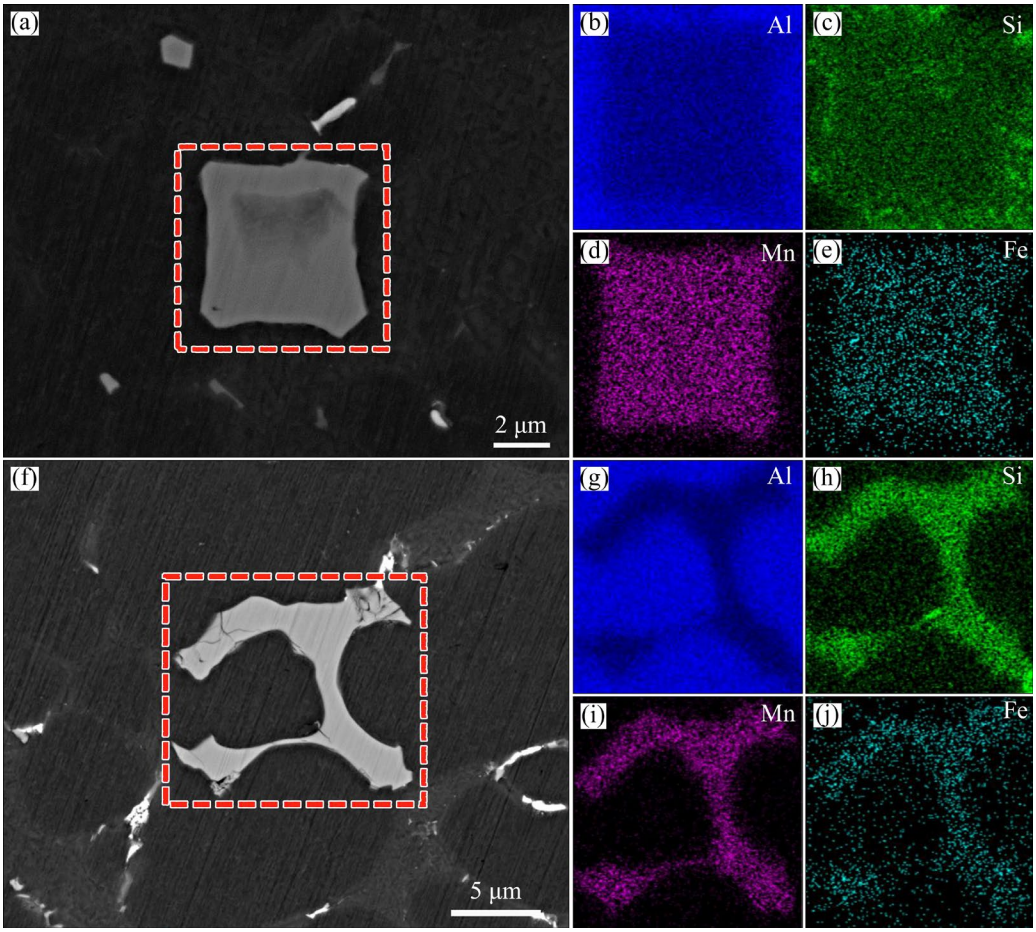

Fig. 8 BSE−SEM images and EDS mappings of primary phases with square-shaped (a−e) and Chinese-script (f−j) morphologies

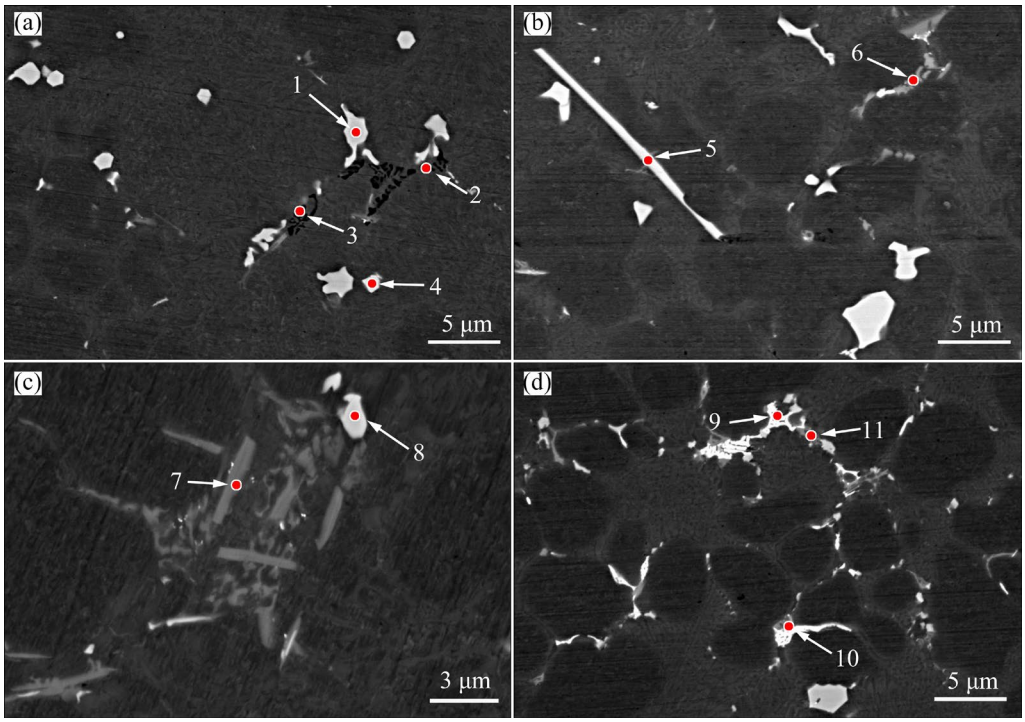

Fig. 9 EDS point analysis results of different primary phases in four as-cast alloys: (a) A1; (b) A2; (c) A3; (d) A4

Table 4 Chemical compositions of intermetallic compounds in four as-cast alloys, identified using SEM−EDS data (at.%)

Point No. in Fig. 9	Al	Si	Mg	Cu	Mn	Fe	Suggested phase
1	69.2	16.1	−	−	13.4	1.2	α-Al(Fe,Mn)Si
2	−	48.9	51.1	−	−	−	β-Mg_2Si
3	−	48.0	52.0	−	−	−	β-Mg_2Si
4	73.1	13.8	−	−	12.2	0.9	α-Al(Fe,Mn)Si
5	69.7	25.9	−	−	3.6	0.8	α-Al(Fe,Mn)Si
6	91.9	3.9	2.8	1.5	−	−	Q-$Al_5Cu_2Mg_8Si_6$
7	58.7	24.9	15.5	1.0	−	−	Q-$Al_5Cu_2Mg_8Si_6$
8	70.5	14.3	−	−	12.5	2.7	α-Al(Fe,Mn)Si
9	75.4	−	−	24.6	−	−	Q-Al_2Cu
10	74.7	−	−	25.3	−	−	Q-Al_2Cu
11	61.3	16.2	15.0	7.5	−	−	Q-$Al_5Cu_2Mg_8Si_6$

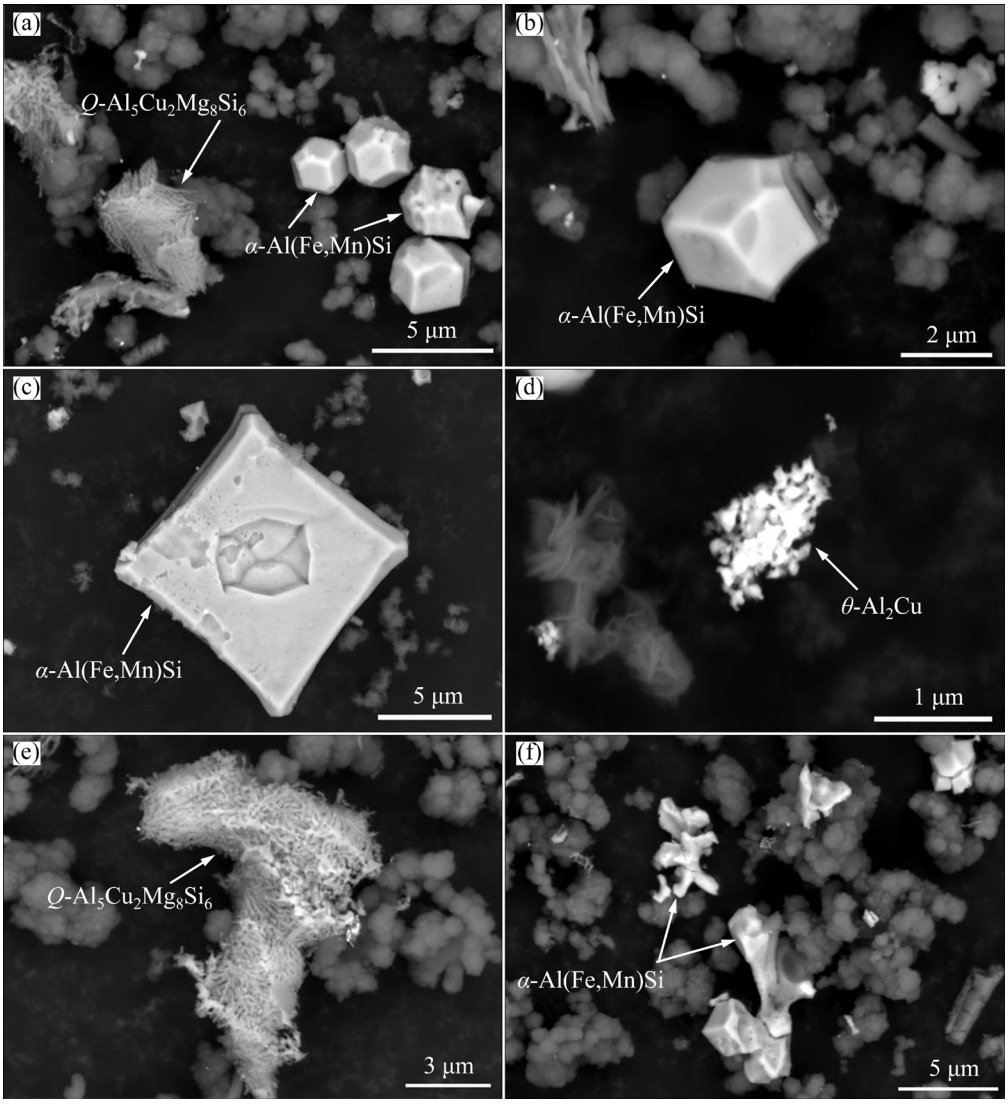

Fig. 10 BSE−SEM images (3D) of samples, revealing different primary phase morphologies compared with 2D analysis: (a) Q-$Al_5Cu_2Mg_8Si_6$ and α-Al(Fe,Mn)Si phases; (b, c, f) α-Al(Fe,Mn)Si phases with skeleton-like, hexahedral and polyhedral morphologies, respectively; (d) θ-Al_2Cu ; (e) Q-$Al_5Cu_2Mg_8Si_6$

found to be different from the 2D morphologies discussed above. The α-Al(Fe,Mn)Si phase with the Chinese-script, square-shaped and polygonal-shaped morphologies in 2D is observed to display the skeleton-like, hexahedral and polyhedral morphologies, respectively, in a 3D view. The θ phase assumes a cotton-like morphology in 3D. The Q phase assumes a flocculent or reticulated morphology. The EDS mappings shown in Fig. 11 confirm that the skeleton-like phase containing Al, Si, Mn and Fe can be identified as the α-Al(Fe,Mn)Si phase, and the cotton-like phase containing Al and Cu can be identify as θ-Al_2Cu. The EDS mappings shown in Fig. 12 link the flocculent-like phase containing Al, Si, Mg and Cu to the Q phase.

The area fractions of the primary phases change with Cu content, as shown in Fig. 13. The

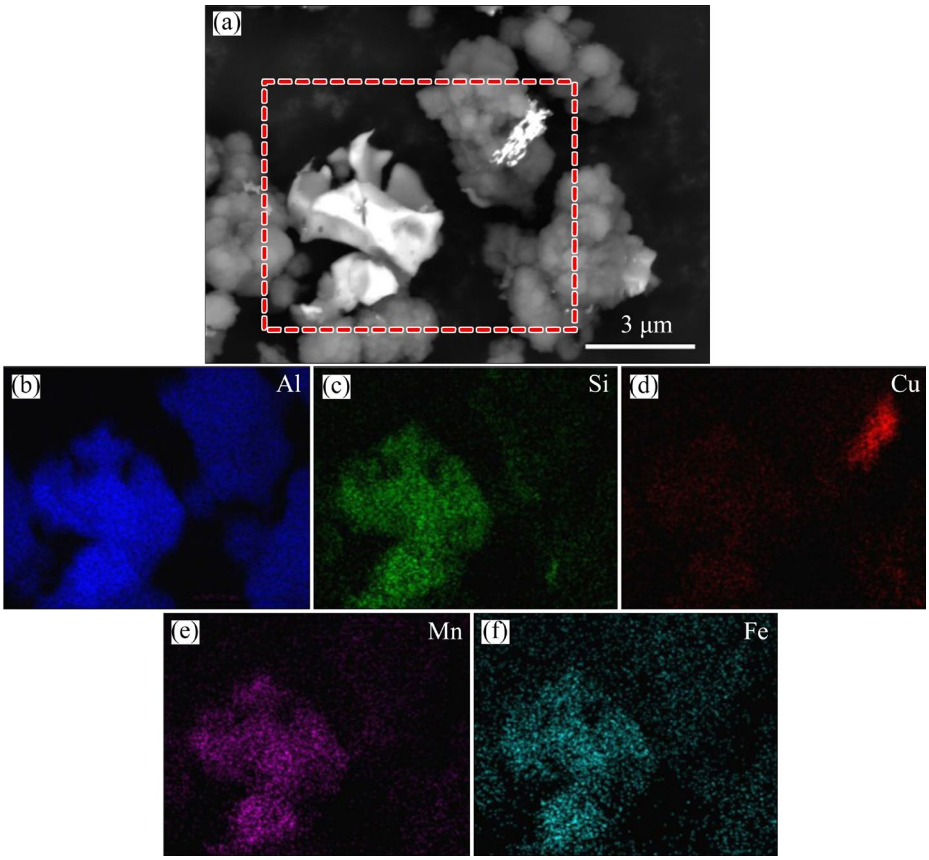

Fig. 11 EDS mappings of two types of primary phases

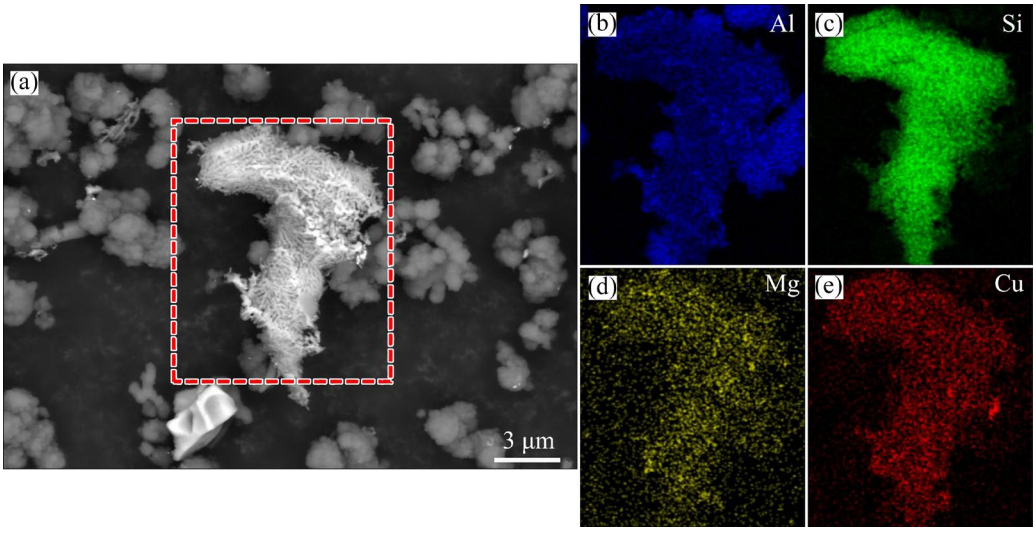

Fig. 12 EDS mappings of one primary phase with flocculent-like morphology

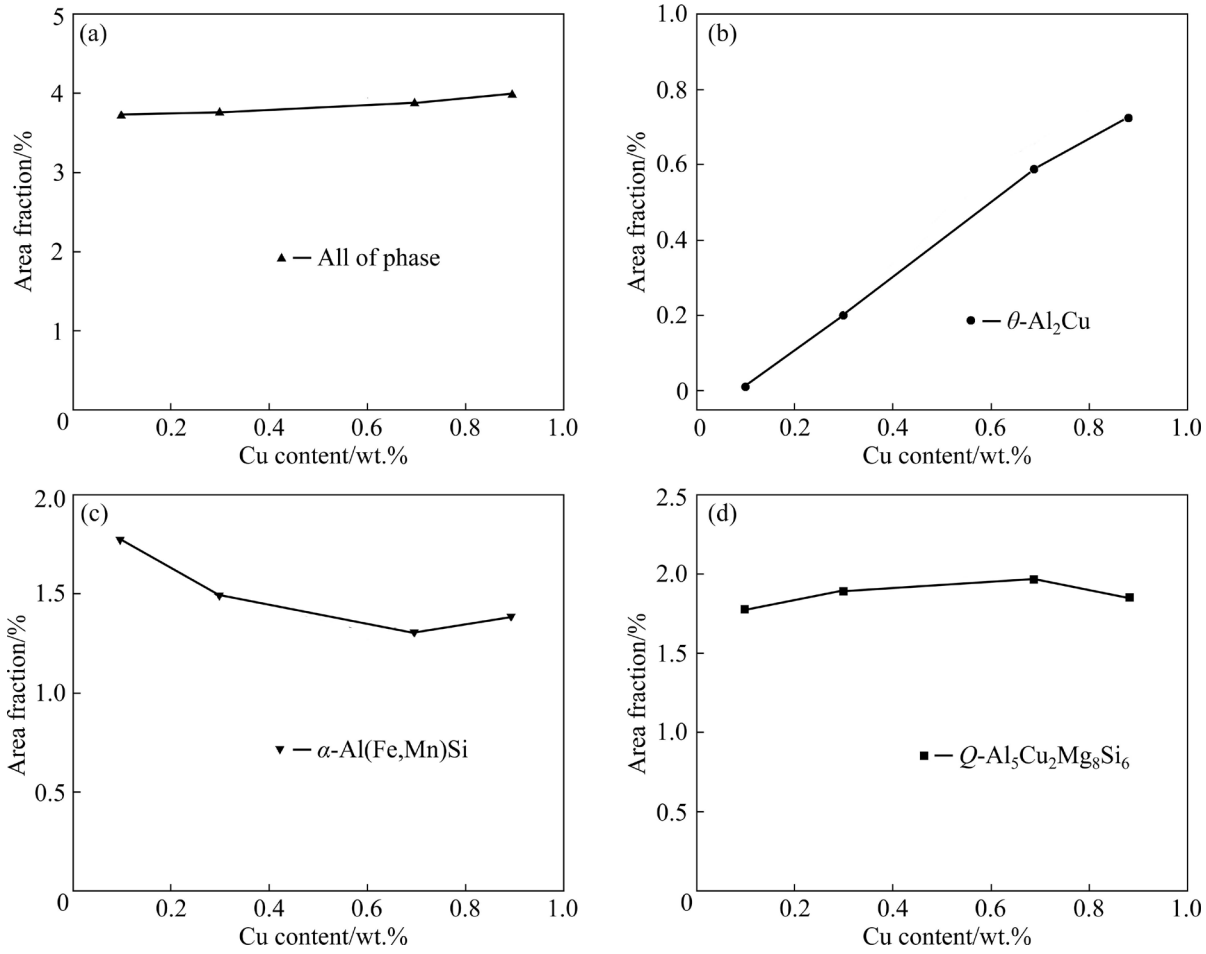

Fig. 13 Change of area fraction of different primary phases in four as-cast alloys with Cu content

total area fractions of these phases are observed to increase slightly with the increase of Cu content (Fig. 13(a)). Figures 13(b−d) show the evolution in the area fractions of the individual phases θ, α-Al(Fe,Mn)Si and Q phases, respectively. The θ phase area fraction rises significantly with increasing Cu content. The α-Al(Fe,Mn)Si phase area fraction decreases initially with increasing Cu content until this content reaches 0.6 wt.%, above which a slight area fraction increase is observed. By contrast, the evolution of the Q phase area fraction displays the opposite trend, with clearly weaker variation. It can be deduced that increasing the Cu content promotes the formation of Cu-containing primary phases, θ and Q, while the decrease of the α-Al(Fe,Mn)Si phase area fraction in response to this alloy composition change is probably due to Si atoms consumed during the formation of the Q phase. The formation of a high density of the θ phase is conducive to the improvement of the alloy strength, at the expense of ductility.

3.2 Microstructure after solution heat treatment

Figure 14 shows the optical metallographic micrographs of four alloys after solution heat treatment at 530 °C for 4 h. Compared with the as-cast alloy, the size, morphology and distribution of the eutectic Si particles have significantly changed. Fragmentation, spheroidization and coarsening of the eutectic Si particles have occurred, and these particles are now uniformly distributed with fine circle-shaped or rod-shaped morphology. In addition, the eutectic Si inter-particle spacing has increased. Apart from Si, some intermetallic compounds can still be observed. These compounds are speculated to be α-Al(Fe,Mn)Si phase particles, given the high temperature stability of this phase. Figure 15 shows SEM images of the four alloys after the solution treatment. The eutectic Si particles have partially dissolved and spheroidized during this treatment. The Q, θ and β phases have completely dissolved into the α(Al) matrix, while the α-Al(Fe,Mn)Si phase has fragmented into

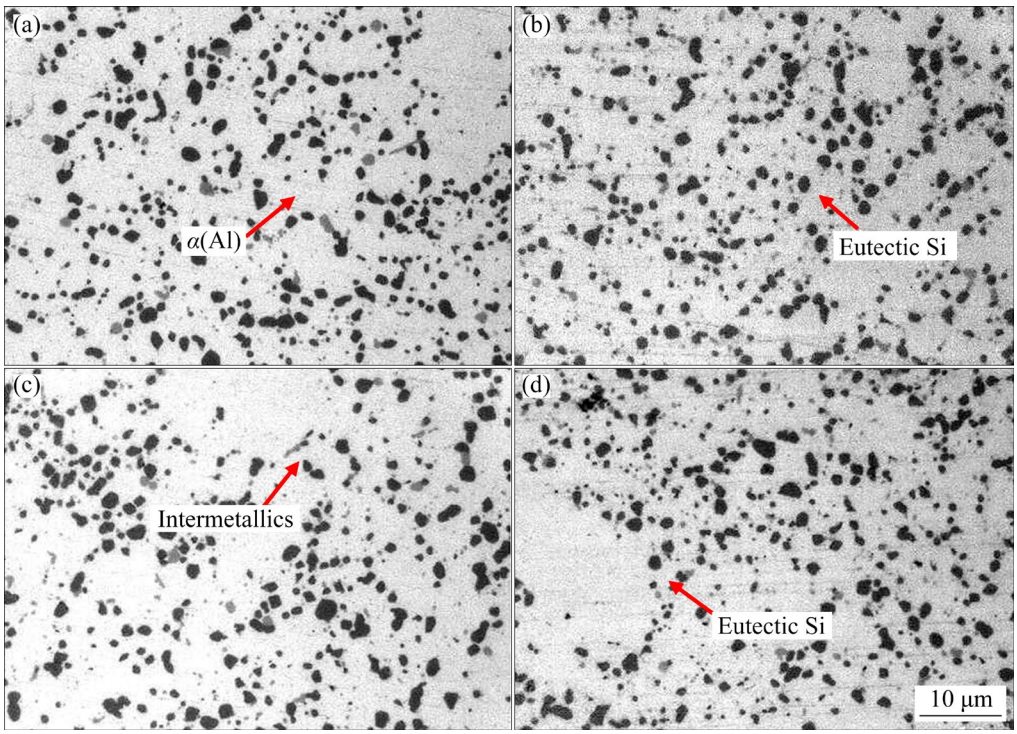

Fig. 14 Optical micrographs of four alloys after solution treatment at 530 °C for 4 h: (a) A1; (b) A2; (c) A3; (d) A4

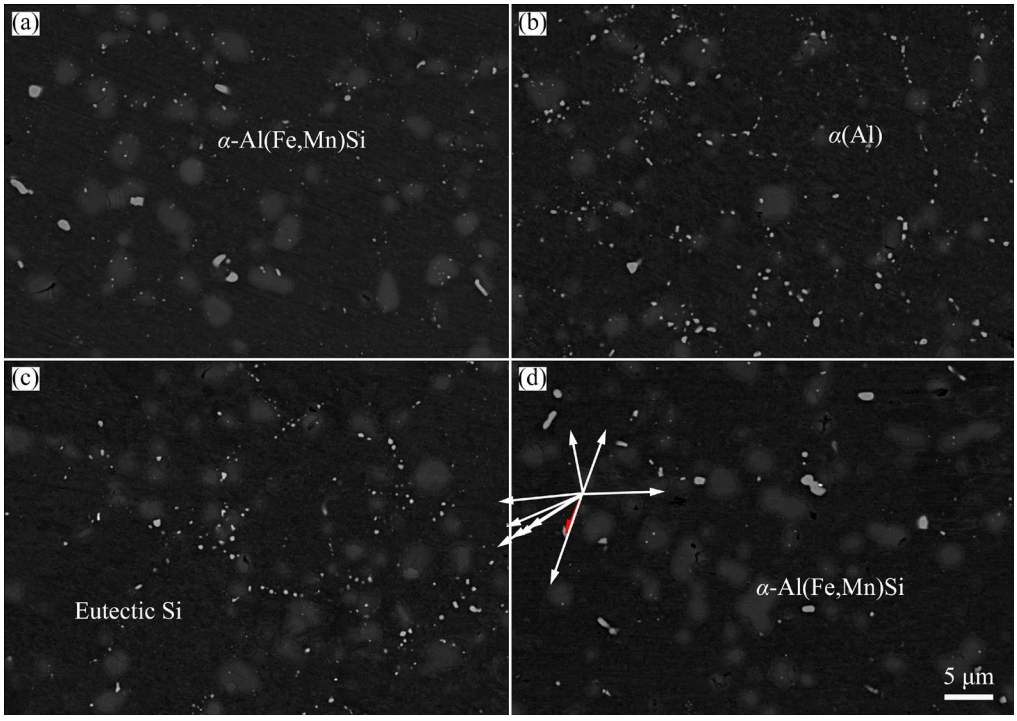

Fig. 15 BSE−SEM images of four alloys after solution treatment at 530 °C for 4 h: (a) A1; (b) A2; (c) A3; (d) A4

fine discontinuous particles dispersed along grain boundaries. The latter evolution is expected to be associated with a reduction of the harmful effect of the α-Al(Fe,Mn)Si phase on the alloy properties.

3.3 Microstructure under peak aging condition

The nano-sized precipitates formed in the four alloys under peak aging condition were characterized by TEM. Figure 16 shows TEM bright-field images of the precipitates acquired

along $\langle 001\rangle_{Al}$ zone axes. Two types of nano-precipitates with dot-like and rod-like morphologies can be observed. These precipitates can be identified as the Q' and θ' phases, based on the HRTEM images shown in Fig. 17. The Q' phase is uniformly distributed in the matrix, and has much higher density than the θ' phase. The average size, area fraction and number density of the Q' and θ' phases in each alloy were quantitatively analyzed, with the results presented in Tables 5 and 6. At least

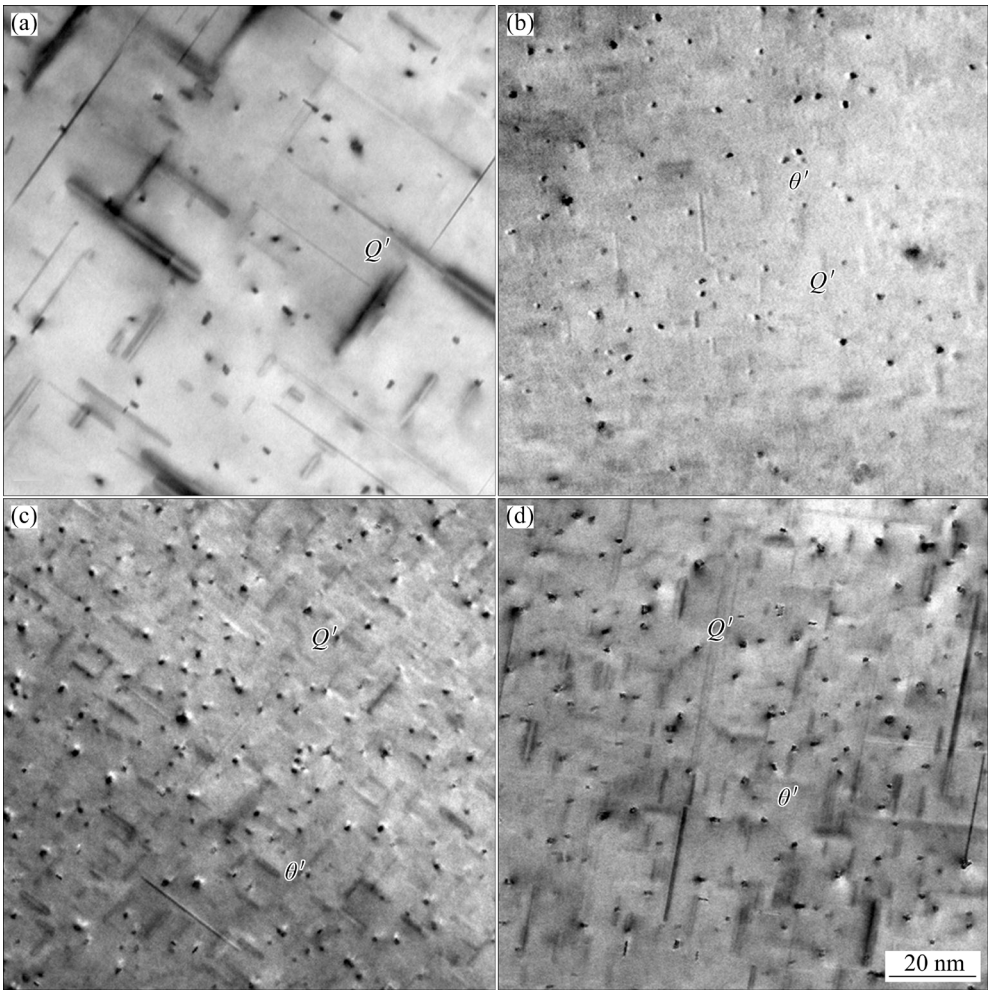

Fig. 16 TEM bright-field images (acquired along $[001]_{Al}$ direction) of four alloys aged at 185 °C for 1 h: (a) A1; (b) A2; (c) A3; (d) A4

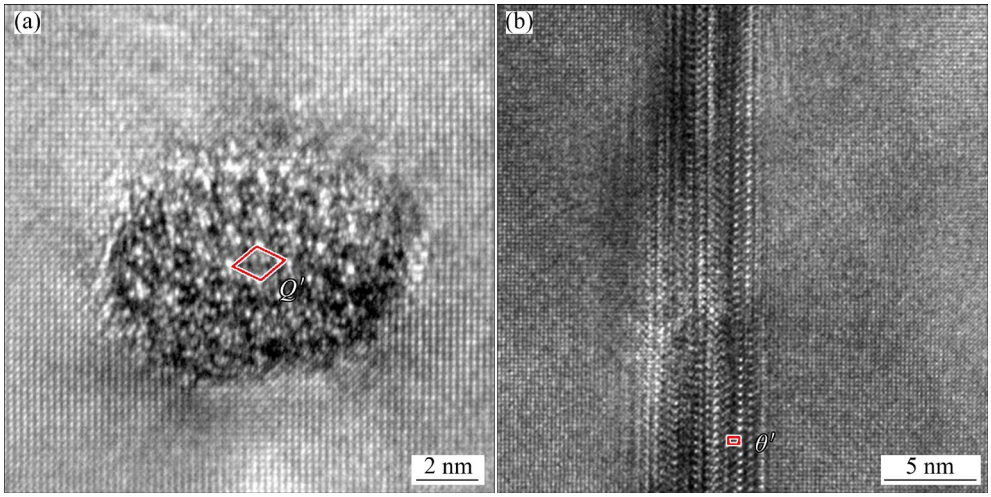

Fig. 17 HRTEM images of Q' (a) and θ' (b) phases (Unit cells of two phases are marked by red lines)

Table 5 Quantitative statistics data for nanoscale precipitate phase (Q') of four alloys aged at 185 °C for 1 h

Alloy	Average diameter/nm	Area fraction/%	Number density/m^{-2}
A1	2.4	1.91	3.76×10^{15}
A2	2.0	2.09	5.18×10^{15}
A3	2.2	2.56	6.38×10^{15}
A4	2.2	4.07	9.69×10^{15}

Table 6 Quantitative statistics data for nanoscale precipitate phase (θ') of four alloys aged at 185 °C for 1 h

Alloy	Average diameter/nm	Area fraction/%	Number density/m^{-2}
A1	–	–	–
A2	3.3	0.64	1.79×10^{14}
A3	2.8	0.75	3.01×10^{14}
A4	3.0	1.17	6.76×10^{14}

ten TEM images were acquired for the sake of producing reliable statistics. In the A1 alloy, only the Q' phase is observed, while Q' and θ' coexist in the A2, A3 and A4 alloys, and the θ' phase density rises with increasing Cu content. The sizes of the Q' and θ' particles change only slightly with increasing Cu content, whereas the number density and area fraction of both phases increase, indicating that the addition of Cu can effectively promote the precipitation of Q' and θ'.

3.4 Hardness

Figure 18(a) shows the microhardness evolution for the four as-cast alloys with respect to alloy Cu content. The hardness increases monotonically with Cu content. The steepness of this increase for the alloys with Cu content above 0.6 wt.% (Alloys A3 and A4) is clearly higher than the values linked to Cu contents below 0.6 wt.%, indicating a growing effect of Cu on Al−Si cast alloy hardness as the Cu content increases. The increasingly sharp rise in hardness with Cu content increase is attributed to the formation of a high number density of Cu-rich primary phases (such as the precursors of the Q and θ phases).

Figure 18(b) shows the hardness evolution of the four alloys during isothermal aging at 185 °C for different holding time, initiated immediately after quenching. The four artificial aging hardness curves display similar trend. The hardness increases rapidly, reaching the peak value after 1 h, followed by a stage of slow decrease and a stable plateau. The peak-aged hardness of the four alloys increases with increasing Cu content, attaining values of HV 128.3 (A1), HV 128.6 (A2), HV 132.3 (A3), and HV 136.8 (A4). This result indicates that Cu addition can promote the alloy precipitation hardening response.

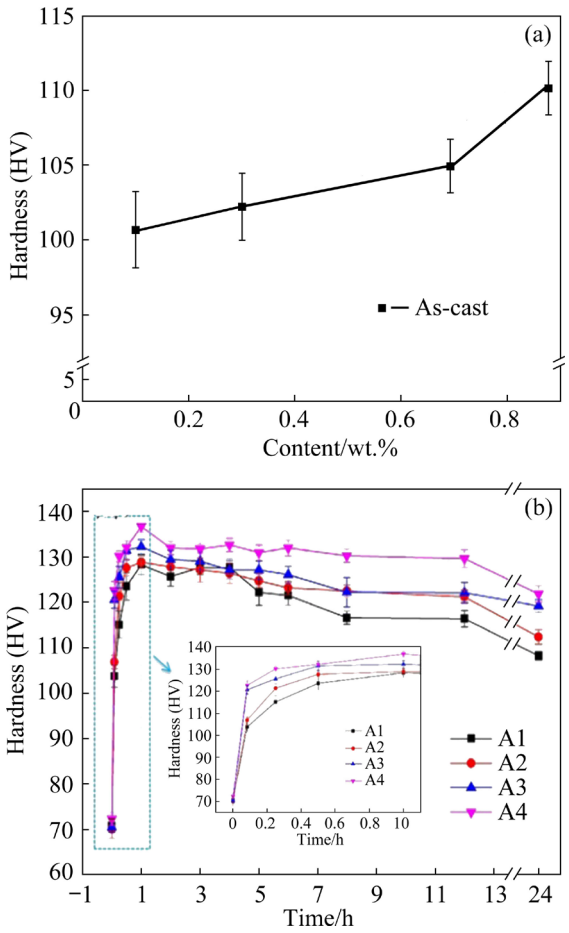

Fig. 18 Hardness evolution with respect to Cu content for four as-cast alloys (a) and hardness evolution for four alloys during artificial aging at 185 °C immediately after quenching (b)

4 Discussion

By systematically investigating the microstructure and properties of the Al−Si−Mg−Mn−xCu alloys under different conditions, it has been demonstrated that the addition of Cu has a series of notable effects on the alloy microstructure. In the as-cast state, porosities represent the most common

defects formed in the alloys. Compared with the conventional cast alloys studied in previous work, the vacuum die cast alloy has a rather low density of small pores, which is beneficial to the alloy properties. However, increasing the Cu content can increase the density of porosity defects in the cast alloys. The formation of these pores can be ascribed to two factors [30]: firstly, the entry of gases due to the rapid filling rate under high pressure; secondly, a large number of coarse primary phases hindering the flow and the feeding of liquid during the solidification process, causing pore formation. The enhancement of porosity induced by Cu is mainly caused by the following factors: (1) Cu introduces a ternary eutectic reaction of Liquid → α(Al) + Si + $CuAl_2$ at about 525 °C, which significantly decreases the solidus and eutectic temperature of the alloy. Therefore, Cu can accumulate to high levels in the eutectic liquid, increasing the volumetric shrinkage during solidification and thus promoting the nucleation of porosities of the alloy [24]. (2) The equilibrium hydrogen gas pressure is increased when Cu is present in the interdendritic liquid, leading to a rapid formation of porosities during solidification in the alloys containing Cu [31].

As for the secondary phase particles, the eutectic Si, α-Al(Fe,Mn)Si and Mg_2Si represent the main primary phases formed in the Al−Si−Mg−Mn alloy. With addition of Cu, the Q-$Al_5Cu_2Mg_8Si_6$ and θ-Al_2Cu phases are formed, and the fractions of these two Cu-containing phases increase with increasing Cu content. Notably, the θ-Al_2Cu phase is only formed in alloys with a Cu content above 0.3 wt.%. By 3D characterization, all the primary phases are shown to exhibit different morphologies. The α-Al(Fe,Mn)Si phase exhibits skeleton-like, hexahedral and polyhedral morphologies, while the θ and Q phases exhibit cotton-like and flocculent/reticulated morphologies, respectively. The 3D characterization results are found to differ notably from the conclusions of a 2D characterization, emphasizing complex and irregular morphologies of these phases. With increasing Cu content, the total area fraction of the full set of primary phases is found to increase slightly. However, the individual primary phases exhibit clearly different evolution trends in response to this alloy composition change. The θ phase area fraction increases significantly. The α-Al(Fe,Mn)Si phase area fraction decreases initially until a Cu content of 0.6 wt.% is reached, above which a slight increase is observed. By comparison, the Q phase area fraction exhibits the opposite trend, with weaker variation. It may be deduced that the addition of Cu can promote the formation of Cu-containing primary phases (θ and Q phases), but with the Q phase formation being limited by the fixed alloy Mg content (0.30−0.35 wt.%), resulting in a comparatively weaker rise in the area fraction with increasing Cu content. The slightly reduced Q phase area fraction in the A4 alloy (Cu content of 0.879 wt.%) is probably due to the formation of the Q phase being suppressed by the θ phase. The area fraction decrease of the α-Al(Fe,Mn)Si phase with increased Cu content is probably due to Si atoms consumed in connection with Q phase formation [31]. Therefore, different primary phases formed in the four cast alloys can significantly affect the mechanical properties of alloys. After solution treatment, the primary phases undergo different evolution paths. The eutectic Si particles are fragmented, spheroidized and partially dissolved, the Q, θ and β phases are completely dissolved in the α(Al) matrix, while the α-Al(Fe,Mn)Si particles are only partially dissolved, indicating the excellent high temperature stability of this latter phase. The dissolution of the Q, θ and β phases in the Al matrix can facilitate the formation of a supersaturated solid solution, promoting precipitation during a subsequent aging treatment. During artificial aging, addition of Cu can significantly increase the alloy hardening kinetics and age hardening response. Firstly, during the early stage of aging, Cu can be incorporated in the Mg−Si co-clusters and refine these clusters due to the strong interaction between Mg and Cu atoms, resulting in accelerated precipitation kinetics [32,33]. Secondly, the addition of Cu suppresses the precipitation of the β'' phase and promotes the formation of the quaternary Q phase and its precursors (Q' phase) during aging. This alteration of the precipitation sequence increases the hardening response of the alloy [34]. Thirdly, for the case of high Cu content alloy, the formation of the nano-sized θ' phase can further increase the alloy hardening potential. The formation of a large number of nano-sized Q' and θ' phases, appearing

in the cast alloys with high Cu content, can significantly improve the mechanical properties of the alloy.

In summary, it has been demonstrated that although the addition of Cu can induce a large number of gas porosity defects in the cast alloys, it could significantly increase the hardness of these alloys under the as-cast, solution and aged conditions. The Cu content in the Al−Si cast alloys should be closely controlled with reference to the desired alloy application performance.

5 Conclusions

(1) The number and size of the gas porosities increase with the increase of Cu content. Additionally, the formation of a considerable amount of Cu-rich eutectic phases facilitates the formation of gas and shrinkage pores.

(2) Five different primary phases are formed in the as-cast alloys, namely eutectic Si, α-Al(Fe,Mn)Si, β-Mg_2Si, Q-$Al_5Cu_2Mg_8Si_6$ and θ-Al_2Cu. An increase of the alloy Cu content can promote the formation of the Cu-containing primary phases, θ and Q. The θ phase starts to form at a Cu content of 0.3 wt.% or above, and its area fraction significantly increases with the increase of Cu content. By contrast, the evolution of the α-Al(Fe,Mn)Si phase area fraction exhibits an inverse trend.

(3) The 3D morphologies of the primary phases are different from the 2D morphologies. The α-Al(Fe,Mn)Si phase with Chinese-script, square-shaped and polygonal-shaped morphologies in 2D is observed to adopt skeleton-like, hexahedral and polyhedral morphologies, respectively, in the 3D view. The θ and Q phases exhibit cotton-like and flocculent/reticulated morphologies, respectively, in 3D view.

(4) Different primary phases undergo different evolution paths during the heat treatment. The eutectic Si particles are fragmented, spheroidized and partially dissolved after solution treatment. The Q, θ and Mg_2Si phases are completely dissolved in the α(Al) matrix, while the α-Al(Fe,Mn)Si phase is only partially dissolved.

(5) The addition of Cu can promote the precipitation hardening response of the cast alloys. The formation of large number of nano-sized Q' and θ' phases during artificial aging is responsible for the high peak aged hardness of the Al−Si cast alloys with high Cu content.

CRediT authorship contribution statement

Zhi-hong JIA: Data curation, Investigation, Writing − Original draft preparation; **Guang-wen ZHOU:** Data curation, Investigation, Review & editing; **Hong-yu ZHOU:** Investigation, Data curation; **Fei LIU:** Conceptualization, Review & editing; **Li-peng DING:** Methodology, Conceptualization, Resources, Writing − Review & editing; **Yao-yao WENG:** Investigation, Review & editing; **Kai-yun XIANG:** Data Curation, Review & editing; **Hai-dong ZHAO:** Conceptualization, Resources, Review & editing.

Declaration of competing interest

The authors declare that they have no known competing financial interests or personal relationships that could have appeared to influence the work reported in this paper.

Acknowledgments

This work was financially supported by the National Key Research and Development Program of China (No. 2020YFA0405903), the National Natural Science Foundation of China (Nos. 52001159, 52101141), and the Natural Science Foundation of Jiangsu Province, China (No. BK20202010). The authors would like to thank Dr. Flemming EHLERS for modifying the English expression of the article.

References

[1] LIU Guang-chen, GAO Jian-bao, CHE Chao, LU Zhao, WANG Yi, ZHANG Li-jun. Optimization of casting means and heat treatment routines for improving mechanical and corrosion resistance properties of A356-0.54Sc casting alloy [J]. Materials Today Communications, 2020, 24: 101227.

[2] HE Yi, XI Hai-hui, MING Wen-quan, SHAO Qin-qin, SHEN Ruo-han, LAI Yu-xiang, WU Cui-lan, CHEN Jiang-hua. Thermal stability and precipitate microstructures of Al−Si−Mg−Er alloy [J]. Transactions of Nonferrous Metals Society of China, 2021, 31: 1−10.

[3] LIU Fei, ZHAO Hai-dong, YANG Run-sheng, SUN Feng-zhen. Microstructure and mechanical properties of high vacuum die-cast AlSiMgMn alloys at as-cast and T6-treated conditions [J]. Materials (Basel), 2019, 12: 2065.

[4] CÁCERES C H, TAYLOR J A. Enhanced ductility in Al−Si−Cu−Mg foundry alloys with high Si content [J]. Metallurgical and Materials Transactions B, 2006, 37: 897−903.

[5] BEROUAL S, BOUMERZOUG Z, PAILLARD P, BORJON-PIRON Y. Effects of heat treatment and addition

of small amounts of Cu and Mg on the microstructure and mechanical properties of Al−Si−Cu and Al−Si−Mg cast alloys [J]. Journal of Alloys and Compounds, 2019, 784: 1026−1035.

[6] KANG H J, YOON P H, LEE G H, PARK J Y, JUNG B J, LEE J Y, LEE C U, KIM E S, CHOI Y S. Evaluation of the gas porosity and mechanical properties of vacuum assisted pore-free die-cast Al−Si−Cu alloy [J]. Vacuum, 2021, 184: 109917.

[7] LIU Ru-xue, ZHENG Jiang, GODLEWSKI L, ZINDEL J, LI Mei, LI Wen-kai, HUANG Shi-yao. Influence of pore characteristics and eutectic particles on the tensile properties of Al−Si−Mn−Mg high pressure die casting alloy [J]. Materials Science and Engineering: A, 2020, 783: 139280.

[8] WANG E R, HUI X D, WANG S S, ZHAO Y F, CHEN G L. Improved mechanical properties in cast Al−Si alloys by combined alloying of Fe and Cu [J]. Materials Science and Engineering: A, 2010, 527: 7878−7884.

[9] SJÖLANDER E, SEIFEDDINE S. The heat treatment of Al−Si−Cu−Mg casting alloys [J]. Journal of Materials Processing Technology, 2010, 210: 1249−1259.

[10] HEIBERG G, NOGITA K, DAHLE A K, ARNBERG L. Columnar to equiaxed transition of eutectic in hypoeutectic aluminium−silicon alloys [J]. Acta Materialia, 2002, 50: 2537−2546.

[11] ALYALDIN L, ABDELAZIZ M H, SAMUEL A M, DOTY H W, VALTIERRA S, SAMUEL F H. Effects of alloying elements and testing temperature on the Q-index of Al−Si based alloys [J]. International Journal of Metalcasting, 2018, 12: 839−852.

[12] CAO X, CAMPBELL J. The solidification characteristics of Fe-rich intermetallics in Al−11.5Si−0.4Mg cast alloys [J]. Metallurgical and Materials Transactions A, 2004, 35: 1425−1435.

[13] YU J M, WANDERKA N, RACK A, DAUDIN R, BOLLER E, MARKÖTTER H, MANZONI A, VOGEL F, ARLT T, MANKE I, BANHART J. Formation of intermetallic δ phase in Al−10Si−0.3Fe alloy investigated by in-situ 4D X-ray synchrotron tomography [J]. Acta Materialia, 2017, 129: 194−202.

[14] WANG Dong-tao, ZHANG Xiao-zu, NAGAUMI H, LI Xin-zhong, ZHANG Hai-tap. 3D morphology and growth mechanism of cubic α-Al(FeMnCr)Si intermetallic in an Al−Si cast alloy [J]. Materials Letters, 2020, 277: 128384.

[15] MATHEW J, REMY G, WILLIAMS M A, TANG Feng-zai, SRIRANGAM P. Effect of Fe intermetallics on microstructure and properties of Al−7Si alloys [J]. JOM, 2019, 71: 4362−4369.

[16] SHABESTARI S G. The effect of iron and manganese on the formation of intermetallic compounds in aluminum-silicon alloys [J]. Materials Science and Engineering: A, 2004, 383: 289−298.

[17] KIM H Y, PARK T Y, HAN S W, LEE H M. Effects of Mn on the crystal structure of α-Al(Mn,Fe)Si particles in A356 alloys [J]. Journal of Crystal Growth, 2006, 291: 207−211.

[18] BISWAS P, PATRA S, ROY H, TIWARY C S, PALIWAL M, MONDAL M K. Effect of Mn addition on the mechanical properties of Al−12.6Si alloy: Role of $Al_{15}(MnFe)_3Si_2$ intermetallic and microstructure modification [J]. Metals and Materials International, 2021, 27: 1713−1727.

[19] MA Z, SAMUEL E, MOHAMED M A, SAMUEL A M, SAMUEL F H, DOTY H W. Influence of aging treatments and alloying additives on the hardness of Al−11Si−2.5Cu−Mg alloys [J]. Materials & Design, 2010, 31: 3791−3803.

[20] DJURDJEVIC M, STOCKWELL T, SOKOLOWSKI J. The effect of strontium on the microstructure of the aluminium−silicon and aluminium−copper eutectics in the 319 aluminium alloy [J]. International Journal of Cast Metals Research, 1999, 12: 67−73.

[21] LI Z, SAMUEL A M, SAMUEL F H, RAVINDRAN C, VALTIERRA S. Effect of alloying elements on the segregation and dissolution of $CuAl_2$ phase in Al−Si−Cu 319 alloys [J]. Journal of Materials Science, 2003, 38: 1203−1218.

[22] XU Cong, MA Chao-li, SUN Yu-feng, HANADA S, LU Guang-xi, GUAN Shao-kang. Optimizing strength and ductility of Al−7Si−0.4 Mg foundry alloy: Role of Cu and Sc addition [J]. Journal of Alloys and Compounds, 2019, 810: 151944.

[23] CÁCERES C H, DJURDJEVIC M B, STOCKWELL T J, SOKOLOWSKI J H. The effect of Cu content on the level of microporosity in Al−Si−Cu−Mg casting alloys [J]. Scripta Materialia, 1999, 40: 631−637.

[24] HWANG J Y, BANERJEE R, DOTY H W, KAUFMAN M J. The effect of Mg on the structure and properties of Type 319 aluminum casting alloys [J]. Acta Materialia, 2009, 57: 1308−1317.

[25] PENG Ji-hua, TANG Xiao-long, HE Jian-ting, XU De-ying. Effect of heat treatment on microstructure and tensile properties of A356 alloys [J]. Transactions of Nonferrous Metals Society of China, 2011, 21: 1950−1956.

[26] TIRYAKIOĞLU M. Si particle size and aspect ratio distributions in an Al−7%Si−0.6%Mg alloy during solution treatment [J]. Materials Science and Engineering: A, 2008, 473: 1−6.

[27] LASA L, RODRIGUEZ-IBABE J M. Evolution of the main intermetallic phases in Al−Si−Cu−Mg casting alloys during solution treatment [J]. Journal of Materials Science, 2004, 39: 1343−1355.

[28] SHAHA S K, CZERWINSKI F, KASPRZAK W, FRIEDMAN J, CHEN D L. Effect of Mn and heat treatment on improvements in static strength and low-cycle fatigue life of an Al−Si−Cu−Mg alloy [J]. Materials Science and Engineering: A, 2016, 657: 441−452.

[29] HUANG Hui-lan, DONG Yan-heng, XING Yuan, JIA Zhi-hong, LIU Qing. Low cycle fatigue behavior at 300 °C and microstructure of Al−Si−Mg casting alloys with Zr and Hf additions [J]. Journal of Alloys and Compounds, 2018, 765: 1253−1262.

[30] YANG Hai-lin, JI Shou-xun, FAN Zhong-yun. Effect of heat treatment and Fe content on the microstructure and mechanical properties of die-cast Al−Si−Cu alloys [J]. Materials & Design, 2015, 85: 823−832.

[31] SHABESTARI S G, MOEMENI H. Effect of copper and solidification conditions on the microstructure and mechanical properties of Al−Si−Mg alloys [J]. Journal of Materials Processing Technology, 2004, 153/154: 193−198.

[32] JIA Z, DING L, CAO L, SANDERS R, LI S, LIU Q. The influence of composition on the clustering and precipitation behavior of Al−Mg−Si−Cu alloys [J]. Metallurgical and Materials Transactions A, 2017, 48: 459−473.
[33] MARCEAU R K W, VAUCORBEIL A, SHA G, RINGER S P, POOLE W J. Analysis of strengthening in AA6111 during the early stages of aging: Atom probe tomography and yield stress modelling [J]. Acta Materialia, 2013, 61: 7285−7303.
[34] DING L P, JIA Z H, NIE J F, WENG Y Y, CAO L F, CHEN H W, WU X Z, LIU Q. The structural and compositional evolution of precipitates in Al−Mg−Si−Cu alloy [J]. Acta Materialia, 2018, 145: 437−450.

Cu 含量和热处理工艺对 Al−Si−Mg−Mn−*x*Cu 铸造铝合金显微组织和力学性能的影响

贾志宏[1,2]，周广文[2]，周宏宇[3]，刘 飞[4]，丁立鹏[1]，翁瑶瑶[5]，向开云[2]，赵海东[4]

1. 南京工业大学 先进轻质高性能材料研究中心，南京 211816；
2. 重庆大学 材料科学与工程学院，重庆 400044；
3. 江苏大学 材料科学与工程学院，镇江 212013；
4. 华南理工大学 国家金属材料近净成形工程技术研究中心，广州 510640；
5. 南京工程学院 材料科学与工程学院，南京 211167

摘 要：采用三维 X 射线显微镜、光学显微镜、扫描电子显微镜、透射电子显微镜及硬度测试系统研究 Cu 含量及热处理工艺对真空压铸 Al−Si−Mg−Mn−*x*Cu 合金显微组织和力学性能的影响。研究发现，虽然 Cu 含量增加会提高铸锭中气孔的密度和尺寸，但是 Cu 添加将促进凝固过程中含 Cu 初生相 (Q-$Al_5Cu_2Mg_8Si_6$ 和 θ-Al_2Cu) 的形成，从而提高合金性能。合金中形成 5 种不同结构的初生相，包括共晶 Si、α-Al(Fe,Mn)Si、β-Mg_2Si、Q-$Al_5Cu_2Mg_8Si_6$ 和 θ-Al_2Cu 相。随着 Cu 含量增加，θ 相的面积分数迅速增加，α-Al(Fe,Mn)Si 相面积分数首先降低，随后缓慢增加，而 Q 相的变化趋势与 α-Al(Fe,Mn)Si 相相反。这些初生相在热处理过程中会出现不同的演变规律。在随后的时效处理过程中，Q'和 θ'相的协同析出能显著提高合金的时效硬化潜力。

关键词：铝硅铸造合金；真空压铸；热处理；显微组织；力学性能；初生相

(Edited by Wei-ping CHEN)